

RIS Position and Orientation Estimation via Multi-Carrier Transmissions and Multiple Receivers

Reza Ghazalian*, Hui Chen[†], George C. Alexandropoulos^{‡§},
Gonzalo Seco-Granados[¶], Henk Wymeersch[†], and Riku Jäntti*

*Aalto University, Finland, [†]Chalmers University of Technology, Sweden,

[‡]National and Kapodistrian University of Athens, Greece, [§]Technology Innovation Institute, UAE,

[¶]Universitat Autònoma de Barcelona, Spain

e-mails: {reza.ghazalian, riku.jantti}@aalto.fi, {hui.chen, henkw}@chalmers.se,
alexandg@di.uoa.gr, gonzalo.seco@uab.cat

Abstract—Reconfigurable intelligent surfaces (RISs) are considered as an enabling technology for the upcoming sixth generation of wireless systems, exhibiting significant potential for radio localization and sensing. An RIS is usually treated as an anchor point with known position and orientation when deployed to offer user localization. However, it can also be attached to a user to enable its localization in a semi-passive manner. In this paper, we consider a static user equipped with an RIS and study the RIS localization problem (i.e., joint three-dimensional position and orientation estimation), when operating in a system comprising a single-antenna transmitter and multiple synchronized single-antenna receivers with known locations. We present a multi-stage estimator using time-of-arrival and spatial frequency measurements, and derive the Cramér-Rao lower bounds for the estimated parameters to validate the estimator's performance. Our simulation results demonstrate the efficiency of the proposed RIS state estimation approach under various system operation parameters.

Index Terms—Localization, reconfigurable intelligent surfaces, orientation, multi-carrier transmission, OFDM, time of arrival.

I. INTRODUCTION

Reconfigurable intelligent surfaces (RISs) are recently considered as a promising paradigm shift for 6G wireless systems [1], [2]. An RIS is a thin planar surface comprising multiple low-cost metamaterials whose response when excited from impinging electromagnetic waves is dynamically programmable [3]. This feature renders RISs as enablers of programmable signal propagation, motivating the concept of smart wireless environments [4], which can be exploited for offering coverage extension as well as localization and mapping [5]. In most cases, RISs are deployed as anchors with known locations and orientations, and can support or enable user localization; this is called *RIS-aided* or *RIS-enabled localization* [6]. In addition, RISs can be carried by a user to enable its semi-passive localization [7]. In this case, the RIS state is unknown and needs to be estimated; this problem is known as *RIS localization* or *RIS state estimation*.

In terms of RIS-aided and RIS-enabled localization, a large number of studies have been conducted ranging from two-dimensional (2D) [8] to three-dimensional (3D) [9] cases, far-field (FF) [10] to near-field (NF) [11] propagation conditions, as well as from indoor [12] to outdoor [13] scenarios. In [8], the authors proposed a method to discriminate the FF from NF targeting the minimization of the user localization error

in an RIS-assisted positioning setup. In [9], the Cramér-Rao lower bounds (CRBs) on the 3D position and orientation of a user for both the NF and FF cases were derived for an RIS-assisted joint communication and localization system. Considering user mobility and the spatial-wideband effect, an efficient localization method was presented for the FF scenario in [10]. An RIS-aided multi-user localization method for an indoor scenario was proposed in [12], where a particle swarm optimization was deployed for the RIS phase profile design. Joint communication and user localization with an RIS mounted on an unmanned aerial vehicle was presented in [13], where the vehicle's trajectory and the RIS phase shifts were jointly optimized. Collectively, all the above works showcase that RISs can boost, or even enable in certain cases, localization, offering improved estimation accuracy with reduced infrastructure cost.

In contrast to RIS-aided or RIS-enabled localization, the problem of *RIS state estimation* is more challenging as a typical passive RIS has no local estimation capabilities, and the problem has received only limited attention. As shown in [7], [14], the localization of an RIS can be formulated as a bi-static sensing problem. In [14], an RIS localization method was developed for a 2D scenario. By using measurements for the time of arrival (TOA), a 3D RIS localization algorithm was proposed in [7]. However, the RIS orientation cannot be estimated from TOA measurements. Note that an RIS contains a planar array of metamaterials, hence, the angle of arrival (AOA) and/or the angle of departure (AOD) information can be exploited for the surface's orientation estimation. However, for an RIS without sensing capabilities and unknown position and orientation, these angles are hard to estimate.

In this paper, we study the RIS joint 3D position and orientation estimation problem under a generic FF channel for the case of a static RIS in the vicinity of multi-carrier transmissions from a single-antenna transmitter (TX) to multiple synchronized single-antenna receivers (RXs). We present a low-complexity estimator based on the measurements at RXs, including the TOA and spatial frequencies at the RIS. To validate its efficiency, we derive the theoretical CRBs for the estimated parameters, which are shown to be achieved under certain operating conditions. We compare the proposed method

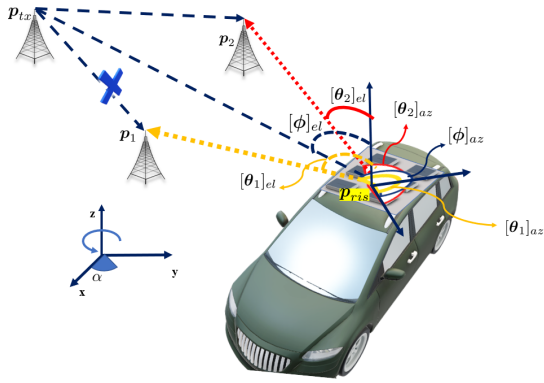


Fig. 1: The considered system model comprising a single-antenna TX, M single-antenna RXs (here, $M = 2$ for illustrational simplicity), and an RIS with unknown 3D position and 1D orientation α (w.r.t. the z axis).

with that in [7] that only uses TOA measurements to show the benefits of exploiting the spatial frequency at the RIS for its orientation estimation.

Notation: Vectors and matrices are indicated by lowercase and uppercase bold letters, respectively. The element in the i th row and j th column of matrix \mathbf{A} is denoted by $[\mathbf{A}]_{i,j}$. The sub-index $i : j$ determines all the elements between i and j . The complex conjugate, Hermitian, transpose, and Moore–Penrose inverse operators are represented by $(\cdot)^*$, $(\cdot)^H$, $(\cdot)^T$, and $(\cdot)^\dagger$, respectively. $\|\cdot\|$ calculates the norm of vectors or Frobenius norm of matrices. By \odot and \otimes , we indicate the element-wise and Kronecker products, respectively. $j = \sqrt{-1}$ and $\mathbf{1}_K$ is a column vector comprising all ones with length K . The functions $\text{atan2}(y, x)$ and $\text{acos}(x)$ are the four-quadrant inverse tangent and inverse cosine functions, respectively.

II. SYSTEM MODEL

In this section, we present the considered wireless system and signal model for the proposed RIS localization problem.

A. System Setup

We consider the multi-carrier downlink transmission system illustrated in Fig. 1, which comprises a single-antenna TX with a known location \mathbf{p}_{tx} , M RXs with known locations $\mathbf{p}_1, \dots, \mathbf{p}_M$, and an RIS with an unknown state, defined as its 3D position \mathbf{p}_{ris} together with its 1D orientation angle α . Note that in this work, we assumed that the RIS only has one orientation degree of freedom. By considering the following rotation matrix:

$$\mathbf{R}_\alpha \triangleq \begin{bmatrix} \cos \alpha & \sin \alpha & 0 \\ -\sin \alpha & \cos \alpha & 0 \\ 0 & 0 & 1 \end{bmatrix}, \quad (1)$$

the direction vectors from the RIS to the TX and to each m th RX in the RIS local coordinate system can be obtained as follows:

$$\mathbf{a}_{\text{tr}} = \mathbf{R}_\alpha \frac{\mathbf{p}_{\text{tx}} - \mathbf{p}_{\text{ris}}}{\|\mathbf{p}_{\text{tx}} - \mathbf{p}_{\text{ris}}\|}, \quad \text{and} \quad \mathbf{a}_{\text{rm}} = \mathbf{R}_\alpha \frac{\mathbf{p}_m - \mathbf{p}_{\text{ris}}}{\|\mathbf{p}_m - \mathbf{p}_{\text{ris}}\|}. \quad (2)$$

The RIS is a uniform planar array with K_r and K_c elements in each row and column, respectively. The inter-element space should be less than half-wavelength $\Delta \leq \lambda/2$, with λ being the signal wavelength. By assuming that the TX and RXs

are synchronized under LOS blockage conditions¹, each RX receives the signals from the TX via the RIS. We assume that the RXs send their measurements to a fusion center [4] to estimate the 3D position and 1D orientation of the RIS.

B. Signal and Channel Models

The TX transmits T orthogonal frequency division multiplexing (OFDM) symbols over time via N_c sub-carriers. We select T sufficiently small such that the considered channel is constant during each transmission interval. Without loss of generality, we assume that all the transmitted symbols over all sub-carriers have unit power. In addition, RIS is programmed to change its phase profile randomly during each discrete time instant t . The RIS phase profile is denoted by vector $\boldsymbol{\gamma}_t \in \mathbb{C}^{K \times 1}$, where $|\boldsymbol{\gamma}_t[k]| = 1 \forall k$ and $K \triangleq K_r K_c$.

After removing the cyclic prefix and computing the fast Fourier transform (FFT), the baseband received signal $\mathbf{Y}_m \in \mathbb{C}^{N_c \times T}$ can be mathematically expressed as:²

$$\mathbf{Y}_m \triangleq g_m \sqrt{P_t} \mathbf{d}(\tau_m) \mathbf{b}^\top(\boldsymbol{\theta}_m, \boldsymbol{\phi}) \boldsymbol{\Gamma} + \mathbf{W}_m, \quad (3)$$

where $g_m \triangleq \rho_m e^{j\varphi_m}$ is an unknown channel gain, and $\boldsymbol{\theta}_m \triangleq [[\boldsymbol{\theta}_m]_{\text{el}}, [\boldsymbol{\theta}_m]_{\text{az}}]^\top$ and $\boldsymbol{\phi} \triangleq [[\boldsymbol{\phi}]_{\text{el}}, [\boldsymbol{\phi}]_{\text{az}}]^\top$ are the AOD from the RIS to the m th RX and the AOA at the RIS from the TX, respectively. In fact, $\boldsymbol{\theta}_m$ is the angle in the direction of vector \mathbf{a}_{rm} , where

$$[\boldsymbol{\theta}_m]_{\text{el}} = \text{acos}([\mathbf{a}_{\text{rm}}]_3) \quad (4)$$

$$[\boldsymbol{\theta}_m]_{\text{az}} = \text{atan2}([\mathbf{a}_{\text{rm}}]_2, [\mathbf{a}_{\text{rm}}]_1). \quad (5)$$

Similarly, $\boldsymbol{\phi}$ is the angle associated with vector \mathbf{a}_{tr} . In addition, P_t denotes the transmission power and $\mathbf{W}_m \in \mathbb{C}^{N_c \times T}$ is the noise matrix containing zero-mean circularly-symmetric independent and identically distributed Gaussian elements with variance³ σ^2 . The delay steering vector $\mathbf{d}(\cdot)$ is defined as follows:

$$\mathbf{d}(\tau_m) \triangleq [1, e^{-j2\pi \Delta f \tau_m}, \dots, e^{-j2\pi (N_c - 1) \Delta f \tau_m}]^\top, \quad (6)$$

where Δf is the sub-carrier spacing. The delay of the propagation path is $\tau_m \triangleq (\|\mathbf{p}_{\text{tx}} - \mathbf{p}_{\text{ris}}\| + \|\mathbf{p}_m - \mathbf{p}_{\text{ris}}\|)/c$ with c being the speed of light. In (3), $\boldsymbol{\Gamma} \triangleq [\boldsymbol{\gamma}(0), \dots, \boldsymbol{\gamma}(T)]^\top$ and $\mathbf{b}(\cdot) \in \mathbb{C}^{K \times 1}$ is the Hadamard product of the RIS array responses from both propagation sides, which is defined as:

$$\mathbf{b}(\boldsymbol{\theta}_m, \boldsymbol{\phi}) \triangleq \mathbf{a}(\boldsymbol{\theta}_m) \odot \mathbf{a}(\boldsymbol{\phi}), \quad (7)$$

where for an arbitrary elevation and azimuth pair $\boldsymbol{\psi}$, we define $\mathbf{a}(\boldsymbol{\psi}) \triangleq \mathbf{a}_r(\boldsymbol{\psi}) \otimes \mathbf{a}_c(\boldsymbol{\psi})$. The n th element of vectors \mathbf{a}_r and \mathbf{a}_c are defined as follows:

$$[\mathbf{a}_r(\boldsymbol{\psi})]_n \triangleq e^{-j \frac{2\pi n \Delta}{\lambda}} \sin[\boldsymbol{\psi}]_{\text{el}} \cos[\boldsymbol{\psi}]_{\text{az}}, \quad n = 0, \dots, K_r - 1 \quad (8a)$$

$$[\mathbf{a}_c(\boldsymbol{\psi})]_n \triangleq e^{-j \frac{2\pi n \Delta}{\lambda}} \sin[\boldsymbol{\psi}]_{\text{el}} \sin[\boldsymbol{\psi}]_{\text{az}}, \quad n = 0, \dots, K_c - 1. \quad (8b)$$

¹Note that, when the LOS path is present, the requirement on TX-RX synchronization can be removed and the approach in [7] can be used for separating the LOS and RIS paths, resulting in this paper's simplified LOS-blockage assumption. However, for the considered synchronized TX and RXs, the LOS path does not convey any information.

²For convenience, we don't consider the LOS path, which, if it is present and resolvable, can be removed from the observation. Since TX and RXs are synchronized, the LOS path provides no additional information.

³We assume that the noise variances at the all RXs are the same. The extension to distinct values for the variances is straightforward.

Considering the latter definition of $\mathbf{a}(\psi)$ and given (7)–(8), the following expression is deduced:

$$\mathbf{b}(\boldsymbol{\theta}_m, \phi) = \mathbf{a}_0(\boldsymbol{\theta}_m, \phi) \otimes \mathbf{a}_1(\boldsymbol{\theta}_m, \phi), \quad (9)$$

where the n th element of $\mathbf{a}_0(\cdot)$ and $\mathbf{a}_1(\cdot)$ can be expressed as:

$$[\mathbf{a}_0(\boldsymbol{\theta}_m, \phi)]_n = e^{-j\frac{2\pi n\Delta}{\lambda}\omega_0(\boldsymbol{\theta}_m, \phi)}, \quad (10a)$$

$$[\mathbf{a}_1(\boldsymbol{\theta}_m, \phi)]_n = e^{-j\frac{2\pi n\Delta}{\lambda}\omega_1(\boldsymbol{\theta}_m, \phi)}, \quad (10b)$$

where we have defined the spatial frequencies

$$\omega_0(\boldsymbol{\theta}_m, \phi) \triangleq \sin[\phi]_{\text{el}} \cos[\phi]_{\text{az}} + \sin[\boldsymbol{\theta}_m]_{\text{el}} \cos[\boldsymbol{\theta}_m]_{\text{az}} \quad (11a)$$

$$\omega_1(\boldsymbol{\theta}_m, \phi) \triangleq \sin[\phi]_{\text{el}} \sin[\phi]_{\text{az}} + \sin[\boldsymbol{\theta}_m]_{\text{el}} \sin[\boldsymbol{\theta}_m]_{\text{az}}. \quad (11b)$$

To ease notation, we hereafter define $\omega_0^m \triangleq \omega_0(\boldsymbol{\theta}_m, \phi)$ and $\omega_1^m \triangleq \omega_1(\boldsymbol{\theta}_m, \phi)$. Accordingly, $\mathbf{b}(\boldsymbol{\theta}_m, \phi)$ can be written as a function of $\boldsymbol{\omega}^m = [\omega_0^m, \omega_1^m]^\top$, i.e., as $\mathbf{b}(\boldsymbol{\omega}^m)$.

Based on the observations (3), we next present an analysis for the considered parameter estimation problem (i.e., the RIS's 3D position and 1D orientation) together with a low-complexity estimation scheme.

III. PROPOSED ESTIMATION METHODOLOGY

In this section, we describe how to estimate the RIS position and orientation from (3), starting with a Fisher information analysis.

A. Fisher Information Analysis

We derive the Fisher information matrix (FIM) and the CRB for the unknown channel (i.e., τ_m , ω_0^m , ω_1^m , ρ_m , and ϕ_m) and RIS-state parameters (i.e., \mathbf{p}_{ris} and α). To this end, we introduce the noise-free part of the observation stacked at the fusion center, say $\mathbf{M} \in \mathbb{C}^{N_c M \times T}$ given (3), (9), (11a), and (11b) as $\mathbf{M} \triangleq [\mathbf{M}_1^\top, \dots, \mathbf{M}_M^\top]^\top$, where $\mathbf{M}_m \triangleq g_m \sqrt{P_t} \mathbf{d}(\tau_m) \mathbf{b}^\top(\boldsymbol{\omega}^m) \boldsymbol{\Gamma} \quad \forall m$. We also introduce the $5M \times 1$ vector with the unknown channel parameters $\boldsymbol{\eta}_{\text{ch}} \triangleq [\boldsymbol{\eta}^\top, \boldsymbol{\rho}^\top, \boldsymbol{\varphi}^\top]^\top$, $\boldsymbol{\eta} \triangleq [\boldsymbol{\tau}^\top, \boldsymbol{\omega}_0^\top, \boldsymbol{\omega}_1^\top]^\top \in \mathbb{R}^{3M \times 1}$, and the 4×1 vector with the RIS state $\boldsymbol{\zeta} \triangleq [\mathbf{p}_{\text{ris}}^\top, \alpha]^\top$, where $\boldsymbol{\tau} \triangleq [\tau_1, \dots, \tau_M]^\top$, $\boldsymbol{\omega}_0 \triangleq [\omega_0^1, \dots, \omega_0^M]^\top$, $\boldsymbol{\omega}_1 \triangleq [\omega_1^1, \dots, \omega_1^M]^\top$, $\boldsymbol{\rho} \triangleq [\rho_0, \dots, \rho_M]^\top$, and $\boldsymbol{\varphi} \triangleq [\varphi_0, \dots, \varphi_M]^\top$. Based on [15, Sec. 3.9], the FIM $\mathbf{J}_{\boldsymbol{\eta}_{\text{ch}}} \in \mathbb{R}^{5M \times 5M}$ is defined as follows:

$$\mathbf{J}_{\boldsymbol{\eta}_{\text{ch}}} \triangleq \frac{2}{\sigma^2} \sum_{t=1}^T \Re \left\{ \left(\frac{\partial [\mathbf{M}]_{:,t}}{\partial \boldsymbol{\eta}_{\text{ch}}} \right)^H \frac{\partial [\mathbf{M}]_{:,t}}{\partial \boldsymbol{\eta}_{\text{ch}}} \right\}. \quad (12)$$

We can then respectively derive the CRB related to τ_m , ω_0^m , and ω_1^m at m th RX, namely, the time error bound (TEB $_m$), the first spatial frequency bound (WEB $_0^m$), and the second spatial frequency bound (WEB $_1^m$) as:

$$\sqrt{\mathbb{E}[(\tau_m - \hat{\tau}_m)^2]} \geq \text{TEB}_m \triangleq \sqrt{[\mathbf{J}_{\boldsymbol{\eta}_{\text{ch}}}^{-1}]_{m,m}}, \quad (13)$$

and for $i \in \{1, 2\}$,

$$\sqrt{\mathbb{E}[(\omega_i^{m-1} - \hat{\omega}_i^{m-1})^2]} \geq \text{WEB}_{i-1}^m \triangleq \sqrt{[\mathbf{J}_{\boldsymbol{\eta}_{\text{ch}}}^{-1}]_{m+iM, m+iM}} \quad (14)$$

where $m \in \{1, \dots, M\}$, and $\hat{\tau}_m$, $\hat{\omega}_0^m$, and $\hat{\omega}_1^m$ are the estimations of the true parameters τ_m , ω_0^m , and ω_1^m , respectively. To derive the FIM of the RIS state, we apply a transformation

from the channel parameter vector $\boldsymbol{\eta}$ to the variables in the state vector $\boldsymbol{\zeta}$. Then, we obtain the equivalent FIM (EFIM) of $\boldsymbol{\eta}$ as $\mathbf{J}_{\boldsymbol{\eta}} = [[\mathbf{J}_{\boldsymbol{\eta}_{\text{ch}}}^{-1}]_{1:3M, 1:3M}]^{-1}$. Accordingly, the FIM of RIS states is defined by means of the transformation matrix $\mathbf{T} \in \mathbb{R}^{3M \times 4}$ (i.e., the Jacobian) as $\mathbf{J}_{\boldsymbol{\zeta}} = \mathbf{T}^\top \mathbf{J}_{\boldsymbol{\eta}} \mathbf{T}$. The ℓ th row and q th entry of \mathbf{T} is defined as [15, eq. (3.30)]:

$$[\mathbf{T}]_{\ell, q} \triangleq \frac{\partial [\boldsymbol{\eta}]_{\ell}}{\partial [\boldsymbol{\zeta}]_q}. \quad (15)$$

The derivations of $\mathbf{J}_{\boldsymbol{\eta}}$ and \mathbf{T} are provided in the Appendix.

Capitalizing on (12) and (15), the desired position error bound (PEB) and orientation error bound (OEB) are computed:

$$\sqrt{\mathbb{E}[\|\hat{\mathbf{p}}_{\text{ris}} - \mathbf{p}_{\text{ris}}\|^2]} \geq \text{PEB} \triangleq \sqrt{\text{tr}([\mathbf{J}_{\boldsymbol{\zeta}}^{-1}]_{1:3, 1:3})}, \quad (16a)$$

$$\sqrt{\mathbb{E}[(\alpha - \hat{\alpha})^2]} \geq \text{OEB} \triangleq \sqrt{[\mathbf{J}_{\boldsymbol{\zeta}}^{-1}]_{4,4}}, \quad (16b)$$

where $\hat{\mathbf{p}}_{\text{ris}}$ and $\hat{\alpha}$ are the estimates of the true RIS position and orientation, respectively.

B. Maximum Likelihood Estimator

We stack all observations at each RX in the matrix \mathbf{Y} , i.e., $\mathbf{Y} \triangleq [\mathbf{Y}_1^\top, \dots, \mathbf{Y}_M^\top]^\top$ and define $\mathbf{g} \triangleq [g_1, \dots, g_M]^\top$. By using the definition of \mathbf{M} and (3)–(11b), we can define the maximum likelihood estimator (MLE) as follows:

$$\begin{aligned} [\hat{\mathbf{g}}, \hat{\alpha}, \hat{\mathbf{p}}_{\text{ris}}] &\triangleq \arg \max_{\mathbf{g}, \alpha, \mathbf{p}_{\text{ris}}} f(\mathbf{Y} | \mathbf{g}, \alpha, \mathbf{p}_{\text{ris}}) \\ &= \arg \min_{\mathbf{g}, \alpha, \mathbf{p}_{\text{ris}}} \|\mathbf{Y} - \mathbf{M}(\mathbf{g}, \alpha, \mathbf{p}_{\text{ris}})\|^2. \end{aligned} \quad (17)$$

To solve (17), we can adopt gradient descent methods (e.g., Newton's method). However, this is challenging since the objective function is non-convex having many local optima. In addition, the gradient descent methods are sensitive to the initial point, i.e., they can get trapped in local optima without appropriate initial points. To this end, we next present a low-complexity estimator to find a proper initial guess.

C. Low-Complexity Estimator

The estimator first estimates the TOA and spatial frequencies at each RIS. Then these estimates are combined to determine the RIS state.

1) *TOA Estimation at each RX*: Let $\mathbf{F} \in \mathbb{C}^{N_F \times N_c}$ be the inverse FFT matrix, defined as $[\mathbf{F}]_{\ell, q} = (1/N_F) e^{j2\pi \ell q / N_F}$. By computing $\mathbf{Z}_m = \mathbf{F} \mathbf{Y}_m$ at each RX, we can coarsely estimate the TOA as $\hat{k}_m \triangleq \arg \max_k \|\mathbf{f}_k^\top \mathbf{Z}_m\|$, where \mathbf{f}_k is a vector comprising all zeros and a one at its k th entry. Next, by solving $\tilde{\delta}_m \triangleq \arg \max_{\delta_m \in [0, 1/(N_F \Delta f)]} \|\mathbf{f}_k^\top \mathbf{F}(\mathbf{Y}_m \odot \mathbf{d}(\delta_m) \mathbf{1}_T)\|$ via the quasi-Newton method using $\delta_m = 0$ as the initial point, a refined TOA estimate τ_m can be obtained [7]:

$$\hat{\tau}_m = \frac{\tilde{k}}{N_F \Delta f} - \tilde{\delta}_m. \quad (18)$$

2) *Estimating $\boldsymbol{\omega}^m$ at each RX*: One can remove the effect of τ_m from \mathbf{Y}_m to obtain the following expression:

$$\begin{aligned} \mathbf{Y}_m^r &= \mathbf{Y}_m \odot (\mathbf{d}(-\hat{\tau}_m) \mathbf{1}_T^\top) \\ &\approx g_m \sqrt{P_t} \mathbf{1}_{N_c} \mathbf{b}^\top(\boldsymbol{\omega}^m) \boldsymbol{\Gamma} + \mathbf{W}_m^d, \end{aligned} \quad (19)$$

where $\mathbf{W}_m^d \triangleq \mathbf{W}_m \odot (\mathbf{d}(-\hat{\tau}_m) \mathbf{1}_T^\top)$. Next, summing \mathbf{Y}_m^r over its rows, and then, computing the transpose, yields:

$$\mathbf{y}_m^r = \mathbf{Y}_m^{r \top} \mathbf{1}_{N_c} = N_c g_m \sqrt{P_t} \boldsymbol{\Gamma}^\top \mathbf{b}(\boldsymbol{\omega}^m) + \mathbf{w}_m^t. \quad (20)$$

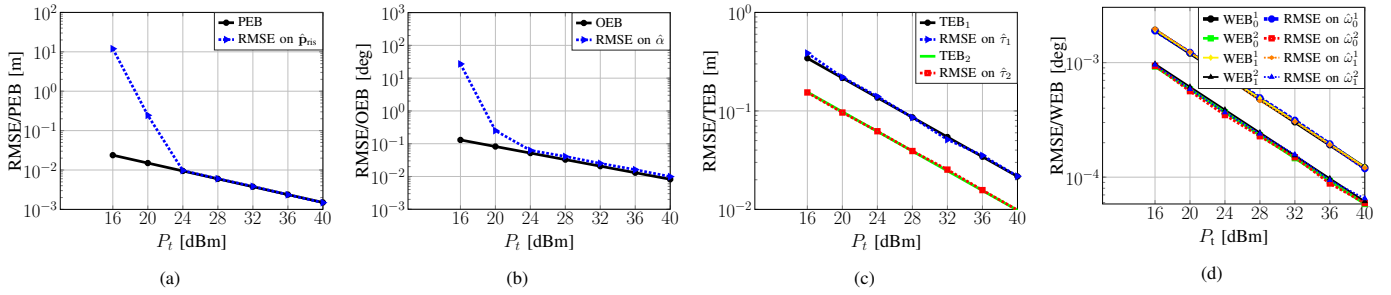


Fig. 2: The evaluation of the RMSE of the estimated channel parameters and RIS state versus the transmit power P_t : (a) RMSE of the RIS position and PEB; (b) RMSE of the RIS orientation (deg) and OEB; (c) RMSE of the TOA and TEB; and (d) RMSE of the ω^m and WEB.

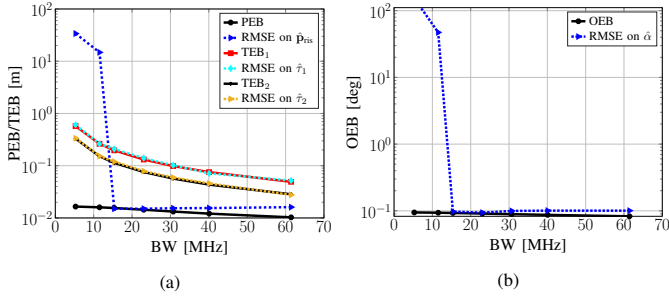


Fig. 3: The effect of the bandwidth (BW) on the estimation accuracy for $P_t = 20$ dBm: (a) RMSE of the RIS position/TOA and PEB; and (b) RMSE of the RIS orientation (deg) and OEB.

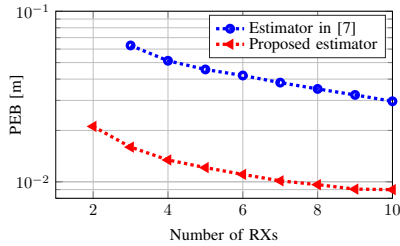


Fig. 4: The comparison of the PEB using only TOA and using TOA along with AOA/AOD information to/from the RIS versus the number of RXs. The RXs are equally distributed on a circle centered at the TX position with a radius equal to 5m; this circle lies on the plane $z = 0$.

Finally, ω^m can be obtained from the MLE estimator:

$$\hat{\omega}^m = \arg \min_{\omega^m} \|\mathbf{y}_m^r - N_c \sqrt{P_t} \hat{g}_m(\omega^m) \mathbf{\Gamma}^\top \mathbf{b}(\omega^m)\|^2, \quad (21)$$

where $\hat{g}_m(\omega^m) \triangleq \mathbf{y}_m^r (\mathbf{\Gamma}^\top \mathbf{b}(\omega^m))^\dagger / (N_c \sqrt{P_t})$. This problem can be solved via a 2D search over the interval $[-2, 2]$, providing a coarse estimation for ω^m . The estimation can be then refined via the quasi-Newton method using the latter coarse estimate as the initial point.

3) *RIS 3D Position and 1D Orientation Estimation*: Using the estimation $\hat{\tau}_m$, the RIS is constrained to lie on the intersection of M spheroids defined as $\|\mathbf{p}_{\text{ris}} - \mathbf{p}_{\text{tx}}\| + \|\mathbf{p}_{\text{ris}} - \mathbf{p}_m\| = c\hat{\tau}_m$. In the general case, the intersection of $M > 2$ spheroids can be found by the method from [7, eq. (16)–(18)]. However, for $M = 2$, this method does not apply, as there is a one-dimensional manifold of solutions. To characterize these, we first mesh the surface of one of the spheroids and then calculate the distances between each of the points on the mesh with the other spheroid, using the technique given in [16, Sec 3]. We finally select the candidate RIS points as the

intersections, which have a distance less than a threshold d_{th} , which is manually set. The resulting set of candidate positions is denoted by \mathcal{P} (where for $M > 2$, this set contains a single point).

By considering that (2) depends on the RIS position and orientation, and substituting the definitions of elevation and azimuth angles (4), (5) in (11), we notice that for a given $\tilde{\mathbf{p}}_{\text{ris}} \in \mathcal{P}$, ω^m is solely a function of α . Hence, $\alpha(\tilde{\mathbf{p}}_{\text{ris}})$ can be found by a line search

$$\hat{\alpha}(\tilde{\mathbf{p}}_{\text{ris}}) = \arg \min_{\alpha \in [0, 2\pi)} \sum_{m=1}^M \|\hat{\omega}^m - \omega^m(\alpha)\|^2. \quad (22)$$

For $M = 2$, we finally find a unique estimate of the position via solving the following optimization problem:

$$\hat{\mathbf{p}}_{\text{ris}} = \arg \min_{\tilde{\mathbf{p}}_{\text{ris}} \in \mathcal{P}} \|\mathbf{y}^r - \mathbf{m}_0(\tilde{\mathbf{p}}_{\text{ris}}, \hat{\alpha}(\tilde{\mathbf{p}}_{\text{ris}}))\|^2, \quad (23)$$

where $\mathbf{y}^r \triangleq \sum_{m=1}^M \mathbf{y}_m^r$, $\mathbf{m}_0(\mathbf{p}_{\text{ris}}, \alpha) \triangleq \sum_{m=1}^M N_c \hat{g}_m(\mathbf{p}_{\text{ris}}, \alpha) \sqrt{P_t} \mathbf{\Gamma}^\top \mathbf{b}(\mathbf{p}_{\text{ris}}, \alpha)$, $\hat{g}_m(\mathbf{p}_{\text{ris}}, \alpha) = \mathbf{y}_m^r (\mathbf{\Gamma}^\top \mathbf{b}(\mathbf{p}_{\text{ris}}, \alpha))^\dagger / (N_c \sqrt{P_t})$. Note that this state estimation can serve as an initial guess the optimization in (17).

IV. NUMERICAL RESULTS

In this section, we evaluate the proposed estimator for $M = 2$ receivers, and compare it with the corresponding bound. In particular, we compare the root mean square error (RMSE) of the estimated parameters with the derived CRBs, using 500 noise realizations. The number of RIS elements was set to $K = 17 \times 17$, and the phase profile of each of them was drawn from the uniform distribution $[0, 2\pi)$. The channel gain

TABLE I: Simulation Parameters.

Parameter	Symbol	Value
Wavelength	λ	1 cm
RIS element spacing	Δ	0.25 cm
Light speed	c	3×10^8 m/sec
Number of sub-carriers	N_c	128
Number of transmissions	T	100
Sub-carrier spacing	Δf	120 kHz
Noise PSD	N_0	-174 dBm/Hz
RX's noise figure	n_f	5 dB
IFFT Size	N_F	4096
The first RX position	\mathbf{p}_1	$[-3\text{m}, 5\text{m}, -1\text{m}]^\top$
The second RX position	\mathbf{p}_2	$[3\text{m}, -3\text{m}, 0\text{m}]^\top$
TX position	\mathbf{p}_{tx}	$[0\text{m}, 0\text{m}, 0\text{m}]^\top$
RIS position	\mathbf{p}_{ris}	$[4\text{m}, 1\text{m}, -4\text{m}]^\top$
RIS orientation	α	$\pi/6$ rad

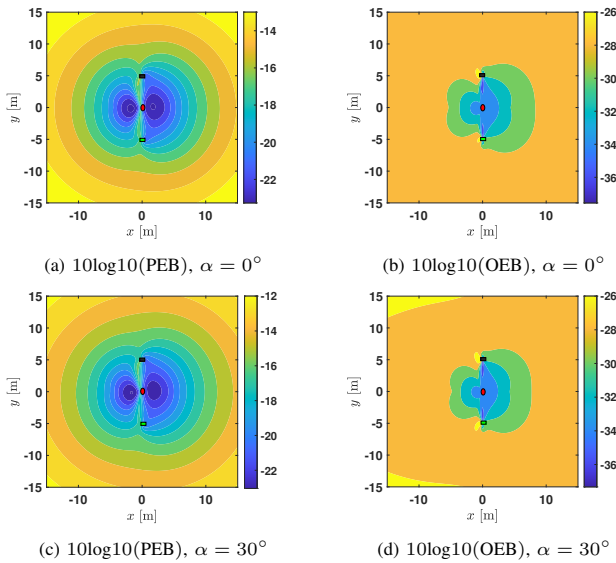


Fig. 5: The contour plots of the PEB and OEB versus the RIS location for one random RIS phase profile and $P_t = 34$ dBm. The TX, first RX, and second RX positions are marked by a red ellipse, green square, and black square, respectively.

$g_m \triangleq \rho_m e^{j\varphi_m}$ modeled with $\varphi_m \sim \mathcal{U}[0, 2\pi)$ and amplitude [17, eqs. (27) and (29)]:

$$\rho_m = \frac{\lambda^2 (\cos[\theta_m]_{\text{el}} \cos[\phi]_{\text{el}})^{0.285}}{16\pi \|\mathbf{p}_{\text{tx}} - \mathbf{p}_{\text{ris}}\| \|\mathbf{p}_m - \mathbf{p}_{\text{ris}}\|}. \quad (24)$$

The rest of the simulation parameters are given in Table I.

A. Results and Discussion

1) *Impact of Transmission Power and Bandwidth:* In Fig. 2, we study the effect of the transmitted power P_t on the performance of the proposed estimator. As shown, the RMSE of channel parameters ($\hat{\tau}_1$, $\hat{\tau}_2$, $\hat{\omega}_0^m$, and $\hat{\omega}_1^m$) and the RIS state ($\hat{\mathbf{p}}_{\text{ris}}$ and $\hat{\alpha}$) are decreasing functions of P_t , and the CRB of the RIS state estimation is attained when $P_t \geq 24$ dBm. It can be also seen that the bottleneck for the RIS state estimation is the TOA estimation at lower transmit power, where a small TOA error leads to a large positioning error. To verify this behavior, we study the effect of the signal bandwidth (BW) in Fig. 3. It is observed that, for low BW values, the localization algorithm fails, whereas more BW yields more accurate TOA estimation.

2) *Gain of Spatial Frequency Estimation over [7]:* In Fig. 4, we compare with the scenario presented in [7], which only estimates the RIS 3D location using TOA. As can be seen, using spatial frequency estimation, which contains AOA/AOD information, along with TOA at RIS, results in a more accurate RIS localization than that using only the TOA. Besides, the estimator proposed in [7] cannot estimate the RIS location with only $M = 2$ RXs, while the proposed method renders the problem identifiable and provides an accurate solution.

3) *Coverage Analysis:* We assess the RIS localization coverage and performance through contour plots of the PEB and OEB in Fig. 5, when the x and y coordinates of the RIS are varying, while its orientation and z coordinate are fixed; we particularly set $z = -1$ m. Two RIS orientations were

considered, namely $\alpha = 0^\circ$ and 30° , and the RXs were located on the ceiling (i.e., the plane $z = 0$) in $[0\text{m}, -5\text{m}, 0\text{m}]^\top$ and $[0\text{m}, 5\text{m}, 0\text{m}]^\top$, respectively. It can be observed that high accurate localization can be obtained when the RIS is close to the TX, due to the high signal-to-noise ratio (SNR). However, one can estimate the RIS orientation with high accuracy when the RIS is located on a line connecting one of the RXs with the TX.

V. CONCLUSION

In this paper, we presented a multi-stage estimator for the 3D position and 1D orientation estimation of an RIS in a multi-carrier system with a single-antenna TX and multiple single-antenna RXs. The proposed estimator leverages the TOA and spatial frequency measurements to estimate the unknown parameters. We showed that the RMSEs of the estimations attain the corresponding CRBs within a specific SNR range. We also demonstrated that using additional measurements, specifically the spatial frequency at the RIS, not only improves the localization accuracy compared to methods using only TOAs, but makes the RIS orientation estimation feasible with even two RXs. In future work, we will investigate the robustness of the estimator to the multipath.

ACKNOWLEDGMENTS

This work has been funded in part by the Academy of Finland Profi-5 under grant number 326346, the ULTRA project under grant number 328215, the EU H2020 RISE-6G project under grant number 10101701, and in part by the Spanish Ministry of Science and Innovation Projects under grant PID2020-118984GB-I00.

APPENDIX

A. Derivation of FIM \mathbf{J}_η

We calculate the term $\partial[\mathbf{M}]_{:,t}/\partial\eta$, using (12), to derive \mathbf{J} . We first define vector $\mathbf{e}_{(m-1)M+1:mM}$ with length M , whose entries from $(m-1)M+1$ to mM are equal to one and the others are equal to zero. To ease notation, we express $(m-1)M+1 : mM$ via m , i.e., \mathbf{e}_m . Given the definition of \mathbf{M} , we have $\partial[\mathbf{M}]_{:,t}/\partial\rho_m = e^{j\varphi_m} \sqrt{P_t} \mathbf{d}(\tau_m) \mathbf{b}(\omega^m) \gamma_t \mathbf{e}_m$, $\partial[\mathbf{M}]_{:,t}/\partial\varphi_m = jg_m \sqrt{P_t} \mathbf{d}(\tau_m) \mathbf{b}(\omega^m) \gamma_t \mathbf{e}_m$, and

$$\frac{\partial[\mathbf{M}]_{:,t}}{\partial\tau_m} = g_m \sqrt{P_t} \frac{\partial\mathbf{d}(\tau_m)}{\partial\tau_m} \mathbf{b}(\omega^m) \gamma_t \mathbf{e}_m, \quad (25)$$

where $\frac{\partial\mathbf{d}(\tau_m)}{\partial\tau_m} = -j2\pi\Delta f g_m (\mathbf{L}_c \odot \mathbf{d}(\tau_m)) \sqrt{P_t} \mathbf{b}(\omega^m) \gamma_t \mathbf{e}_m$ and $\mathbf{L}_c \triangleq ([0, \dots, M-1]^\top)^\top$. In addition, for $i = 0$ and 1 , we have the derivatives:

$$\frac{\partial[\mathbf{M}]_{:,t}}{\partial\omega_i^m} = g_m \mathbf{d}(\tau_m) \sqrt{P_t} \frac{\partial\mathbf{b}^\top(\omega^m)}{\partial\omega_i^m} \gamma_t \mathbf{e}_m, \quad (26)$$

where $\frac{\partial\mathbf{b}(\omega^m)}{\partial\omega_0^m} = -j2\pi\Delta/\lambda (\mathbf{L} \otimes \mathbf{1}) \odot \mathbf{b}(\omega^m)$, $\frac{\partial\mathbf{b}(\omega^m)}{\partial\omega_1^m} = -j2\pi\Delta/\lambda (\mathbf{1} \otimes \mathbf{L}) \odot \mathbf{b}(\omega^m)$, and $\mathbf{L} \triangleq [-\frac{M-1}{2}, \dots, \frac{M-1}{2}]^\top$.

B. Derivation of Jacobian Matrix \mathbf{T}

To calculate \mathbf{T} , we first define the auxiliary variables $\mathbf{u}_A \triangleq (\mathbf{p}_{\text{tx}} - \mathbf{p}_{\text{ris}})/\|\mathbf{p}_{\text{tx}} - \mathbf{p}_{\text{ris}}\|$ and $\mathbf{u}_{D,m} \triangleq (\mathbf{p}_m - \mathbf{p}_{\text{ris}})/\|\mathbf{p}_m - \mathbf{p}_{\text{ris}}\|$, as well as $\mathbf{R}_\alpha = [\mathbf{r}_1, \mathbf{r}_2, \mathbf{r}_3]^\top$ in (1)

with $\mathbf{r}_1 \triangleq [\cos \alpha, -\sin \alpha, 0]^\top$, $\mathbf{r}_2 \triangleq [\sin \alpha, \cos \alpha, 0]^\top$, and $\mathbf{r}_3 \triangleq [0, 0, 1]^\top$. Using these variables, we can rewrite AOA and AODs as follows [18, Appendix A]:

$$\phi = [\text{atan2}(\mathbf{r}_2^\top \mathbf{u}_A, \mathbf{r}_1^\top \mathbf{u}_A), \text{acos}(\mathbf{r}_3^\top \mathbf{u}_A)]^\top, \quad (27a)$$

$$\theta_m = [\text{atan2}(\mathbf{r}_2^\top \mathbf{u}_{D,m}, \mathbf{r}_1^\top \mathbf{u}_{D,m}), \text{acos}(\mathbf{r}_3^\top \mathbf{u}_{D,m})]^\top, \quad (27b)$$

In the sequel, we compute the derivatives:

$$\frac{\partial \mathbf{u}_A}{\partial \mathbf{p}_{\text{ris}}} = (\mathbf{u}_A \mathbf{u}_A^\top - \mathbf{I}_3) / \|\mathbf{p}_{\text{tx}} - \mathbf{p}_{\text{ris}}\|, \quad (28a)$$

$$\frac{\partial \mathbf{u}_{D,m}}{\partial \mathbf{p}_{\text{ris}}} = (\mathbf{u}_{D,m} \mathbf{u}_{D,m}^\top - \mathbf{I}_3) / \|\mathbf{p}_m - \mathbf{p}_{\text{ris}}\|, \quad (28b)$$

$$\frac{\partial [\phi]_{\text{az}}}{\partial \mathbf{u}_A} = \frac{(\mathbf{r}_1^\top \mathbf{u}_A) \mathbf{r}_2 - (\mathbf{r}_2^\top \mathbf{u}_A) \mathbf{r}_1}{(\mathbf{r}_1^\top \mathbf{u}_A)^2 + (\mathbf{r}_2^\top \mathbf{u}_A)^2}, \quad (28c)$$

$$\frac{\partial [\phi]_{\text{el}}}{\partial \mathbf{u}_A} = \frac{-\mathbf{r}_3}{\sqrt{(1 - \mathbf{r}_3^\top \mathbf{u}_A)}}, \quad (28d)$$

$$\frac{\partial [\theta_m]_{\text{az}}}{\partial \mathbf{u}_{D,m}} = \frac{(\mathbf{r}_1^\top \mathbf{u}_{D,m}) \mathbf{r}_2 - (\mathbf{r}_2^\top \mathbf{u}_{D,m}) \mathbf{r}_1}{(\mathbf{r}_1^\top \mathbf{u}_{D,m})^2 + (\mathbf{r}_2^\top \mathbf{u}_{D,m})^2}, \quad (28e)$$

$$\frac{\partial [\theta_m]_{\text{el}}}{\partial \mathbf{u}_{D,m}} = \frac{-\mathbf{r}_3}{\sqrt{(1 - \mathbf{r}_3^\top \mathbf{u}_{D,m})}}, \quad (28f)$$

$$\frac{\partial [\phi]_{\text{az}}}{\partial \alpha} = \frac{(\mathbf{r}_1^\top \mathbf{u}_A) \mathbf{r}_2^\top \mathbf{u}_A - (\mathbf{r}_2^\top \mathbf{u}_A) \mathbf{r}_1^\top \mathbf{u}_A}{(\mathbf{r}_1^\top \mathbf{u}_A)^2 + (\mathbf{r}_2^\top \mathbf{u}_A)^2}, \quad (28g)$$

$$\frac{\partial [\theta_m]_{\text{az}}}{\partial \alpha} = \frac{(\mathbf{r}_1^\top \mathbf{u}_{D,m}) \mathbf{r}_2^\top \mathbf{u}_{D,m} - (\mathbf{r}_2^\top \mathbf{u}_{D,m}) \mathbf{r}_1^\top \mathbf{u}_{D,m}}{(\mathbf{r}_1^\top \mathbf{u}_{D,m})^2 + (\mathbf{r}_2^\top \mathbf{u}_{D,m})^2}, \quad (28h)$$

where $\mathbf{r}'_1 \triangleq [-\sin \alpha, -\cos \alpha, 0]^\top$, $\mathbf{r}'_2 \triangleq [\cos \alpha, -\sin \alpha, 0]^\top$, and $\mathbf{r}'_3 \triangleq [0, 0, 0]^\top$. Using (11a) and (11b), we can easily find $\partial \omega_0^m / \partial [\phi]_{\text{az}}$, $\partial \omega_0^m / \partial [\phi]_{\text{el}}$, $\partial \omega_1^m / \partial [\phi]_{\text{az}}$, $\partial \omega_1^m / \partial [\phi]_{\text{el}}$, $\partial \omega_0^m / \partial [\theta_m]_{\text{az}}$, $\partial \omega_0^m / \partial [\theta_m]_{\text{el}}$, $\partial \omega_1^m / \partial [\theta_m]_{\text{az}}$, and $\partial \omega_1^m / \partial [\theta_m]_{\text{el}}$, which we have not brought in the paper due to page limit. Using the variables in (27a)–(28h), results in:

$$\mathbf{T}_{m,1:3} = \frac{\partial \tau_m}{\partial \mathbf{p}_{\text{ris}}} = \frac{\mathbf{u}_A + \mathbf{u}_{D,m}}{c} \quad \forall m = \{1, \dots, M\}, \quad (29a)$$

$$\begin{aligned} \mathbf{T}_{m,1:3} &= \frac{\partial \omega_0^m}{\partial \mathbf{p}_{\text{ris}}} = \left(\frac{\partial \omega_0^m}{\partial [\phi]_{\text{az}}} \frac{\partial [\phi]_{\text{az}}}{\partial \mathbf{u}_A} + \frac{\partial \omega_0^m}{\partial [\phi]_{\text{el}}} \frac{\partial [\phi]_{\text{el}}}{\partial \mathbf{u}_A} \right) \frac{\partial \mathbf{u}_A}{\partial \mathbf{p}_{\text{ris}}} \\ &+ \left(\frac{\partial \omega_0^m}{\partial [\theta_m]_{\text{el}}} \frac{\partial [\theta_m]_{\text{el}}}{\partial \mathbf{u}_{D,m}} + \frac{\partial \omega_0^m}{\partial [\theta_m]_{\text{az}}} \frac{\partial [\theta_m]_{\text{az}}}{\partial \mathbf{u}_{D,m}} \right) \frac{\partial \mathbf{u}_{D,m}}{\partial \mathbf{p}_{\text{ris}}} \\ &\quad \forall m = \{1 + M, \dots, 2M\}, \end{aligned} \quad (29b)$$

$$\begin{aligned} \mathbf{T}_{m,1:3} &= \frac{\partial \omega_1^m}{\partial \mathbf{p}_{\text{ris}}} = \left(\frac{\partial \omega_1^m}{\partial [\phi]_{\text{az}}} \frac{\partial [\phi]_{\text{az}}}{\partial \mathbf{u}_A} + \frac{\partial \omega_1^m}{\partial [\phi]_{\text{el}}} \frac{\partial [\phi]_{\text{el}}}{\partial \mathbf{u}_A} \right) \frac{\partial \mathbf{u}_A}{\partial \mathbf{p}_{\text{ris}}} \\ &+ \left(\frac{\partial \omega_1^m}{\partial [\theta_m]_{\text{el}}} \frac{\partial [\theta_m]_{\text{el}}}{\partial \mathbf{u}_{D,m}} + \frac{\partial \omega_1^m}{\partial [\theta_m]_{\text{az}}} \frac{\partial [\theta_m]_{\text{az}}}{\partial \mathbf{u}_{D,m}} \right) \frac{\partial \mathbf{u}_{D,m}}{\partial \mathbf{p}_{\text{ris}}} \\ &\quad \forall m = \{1 + 2M, \dots, 3M\}, \end{aligned} \quad (29c)$$

Finally, considering (28g)–(28h), we have:

$$\begin{aligned} \mathbf{T}_{m,4} &= \frac{\partial \omega_0^m}{\partial \alpha} = \frac{\partial \omega_0^m}{\partial [\phi]_{\text{az}}} \frac{\partial [\phi]_{\text{az}}}{\partial \alpha} + \frac{\partial \omega_0^m}{\partial [\theta_m]_{\text{az}}} \frac{\partial [\theta_m]_{\text{az}}}{\partial \alpha} \\ &\quad \forall m = \{1 + M, \dots, 2M\}, \end{aligned} \quad (30a)$$

$$\begin{aligned} \mathbf{T}_{m,4} &= \frac{\partial \omega_1^m}{\partial \alpha} = \frac{\partial \omega_1^m}{\partial [\phi]_{\text{az}}} \frac{\partial [\phi]_{\text{az}}}{\partial \alpha} + \frac{\partial \omega_1^m}{\partial [\theta_m]_{\text{az}}} \frac{\partial [\theta_m]_{\text{az}}}{\partial \alpha} \\ &\quad \forall m = \{1 + 2M, \dots, 3M\}, \end{aligned} \quad (30b)$$

and the remaining elements of \mathbf{T} are zero.

REFERENCES

- [1] C. Huang, A. Zappone, G. C. Alexandropoulos, M. Debbah, and C. Yuen, "Reconfigurable intelligent surfaces for energy efficiency in wireless communication," *IEEE transactions on wireless communications*, vol. 18, no. 8, pp. 4157–4170, 2019.
- [2] M. D. Renzo, M. Debbah, D.-T. Phan-Huy, A. Zappone, M.-S. Alouini, C. Yuen, V. Sciancalepore, G. C. Alexandropoulos, J. Hoydis, H. Gacanin *et al.*, "Smart radio environments empowered by reconfigurable AI meta-surfaces: An idea whose time has come," *EURASIP Journal on Wireless Communications and Networking*, vol. 2019, no. 1, pp. 1–20, 2019.
- [3] M. Jian, G. C. Alexandropoulos, E. Basar, C. Huang, R. Liu, Y. Liu, and C. Yuen, "Reconfigurable intelligent surfaces for wireless communications: Overview of hardware designs, channel models, and estimation techniques," *Intelligent and Converged Networks*, vol. 3, no. 1, pp. 1–32, 2022.
- [4] E. C. Strinati, G. C. Alexandropoulos, H. Wymeersch, B. Denis, V. Sciancalepore, R. D'Errico, A. Clemente, D.-T. Phan-Huy, E. De Carvalho, and P. Popovski, "Reconfigurable, intelligent, and sustainable wireless environments for 6G smart connectivity," *IEEE Communications Magazine*, vol. 59, no. 10, pp. 99–105, 2021.
- [5] H. Wymeersch, J. He, B. Denis, A. Clemente, and M. Juntti, "Radio localization and mapping with reconfigurable intelligent surfaces: Challenges, opportunities, and research directions," *IEEE Vehicular Technology Magazine*, vol. 15, no. 4, pp. 52–61, 2020.
- [6] K. Keykhosravi, B. Denis, G. C. Alexandropoulos, Z. S. He, A. Albanese, V. Sciancalepore, and H. Wymeersch, "Leveraging ris-enabled smart signal propagation for solving infeasible localization problems," *arXiv preprint arXiv:2204.11538*, 2022.
- [7] K. Keykhosravi, M. F. Keskin, S. Dwivedi, G. Seco-Granados, and H. Wymeersch, "Semi-passive 3D positioning of multiple RIS-enabled users," *IEEE Transactions on Vehicular Technology*, vol. 70, no. 10, pp. 11 073–11 077, 2021.
- [8] S. Huang, B. Wang, Y. Zhao, and M. Luan, "Near-field RSS-based localization algorithms using reconfigurable intelligent surface," *IEEE Sensors Journal*, vol. 22, no. 4, pp. 3493–3505, 2022.
- [9] A. Elzanaty, A. Guerra, F. Guidi, and M.-S. Alouini, "Reconfigurable intelligent surfaces for localization: Position and orientation error bounds," *IEEE Transactions on Signal Processing*, vol. 69, pp. 5386–5402, 2021.
- [10] K. Keykhosravi, M. F. Keskin, G. Seco-Granados, P. Popovski, and H. Wymeersch, "Ris-enabled siso localization under user mobility and spatial-wideband effects," *IEEE Journal of Selected Topics in Signal Processing*, vol. 16, no. 5, pp. 1125–1140, 2022.
- [11] Z. Abu-Shaban, K. Keykhosravi, M. F. Keskin, G. C. Alexandropoulos, G. Seco-Granados, and H. Wymeersch, "Near-field localization with a reconfigurable intelligent surface acting as lens," in *Proc. IEEE ICC*, 2021.
- [12] H. Zhang, H. Zhang, B. Di, K. Bian, Z. Han, and L. Song, "Metalocalization: Reconfigurable intelligent surface aided multi-user wireless indoor localization," *IEEE Transactions on Wireless Communications*, vol. 20, no. 12, pp. 7743–7757, 2021.
- [13] J. Luo, T. Liang, C. Chen, and T. Zhang, "A UAV mounted RIS aided communication and localization integration system for ground vehicles," in *Proc. IEEE ICC Workshops*, 2022.
- [14] R. Ghazalian, K. Keykhosravi, H. Chen, H. Wymeersch, and R. Jäntti, "Bi-static sensing for near-field ris localization," in *Proc. IEEE GLOBECOM*, 2022.
- [15] S. M. Kay, *Fundamentals of statistical signal processing: estimation theory*. Prentice-Hall, Inc., 1993.
- [16] D. Eberly, "Distance from a point to an ellipse, an ellipsoid, or a hyperellipsoid," *Preprint*, see <http://www.geometricaltools.com>, vol. 2, 2013.
- [17] S. W. Ellingson, "Path loss in reconfigurable intelligent surface-enabled channels," in *Proc. IEEE PIMRC*, 2021.
- [18] M. A. Nazari, G. Seco-Granados, P. Johannisson, and H. Wymeersch, "Mmwave 6D radio localization with a snapshot observation from a single bs," *arXiv preprint arXiv:2204.05189*, 2022.